Nanoscale Advances

ROYAL SOCIETY OF CHEMISTRY

PAPER

View Article Online
View Journal | View Issue

Cite this: *Nanoscale Adv.*, 2025, **7**, 7246

Palladium-containing magnetic UiO-66–NH_2 as a highly powerful and recoverable nanocatalyst for the reduction of nitrobenzenes

Shiva Kargar and Dawood Elhamifar *

Received 3rd June 2025
Accepted 8th September 2025

DOI: 10.1039/d5na00543d

rsc.li/nanoscale-advances

Magnetically recoverable porous materials with tunable surface chemistry are of growing interest for heterogeneous catalysis due to their ease of separation, structural versatility, and high surface accessibility. However, integrating multiple functional components into a single stable and reusable catalytic platform remains a significant challenge. In this study, the design and synthesis of a hierarchical nanocomposite, Fe_3O_4@MCM-41@UiO-66/SB–Pd, through a stepwise functionalization approach are reported. The strategy integrates a magnetic Fe_3O_4 core, mesoporous silica, a microporous UiO-66–NH_2 framework, and a Schiff base-coordinated Pd complex to yield a structurally ordered and catalytically active nanocomposite. The resulting nanomaterial exhibited a high surface area (249.1 m^2 g^{-1}), hierarchical porosity, thermal stability, and superparamagnetic behavior. Comprehensive characterization confirmed the successful incorporation of all functional groups while maintaining crystallinity. The Fe_3O_4@MCM-41@UiO-66/SB–Pd nanocomposite demonstrated high catalytic efficiency for the reduction of nitroarenes under mild conditions, along with excellent reusability. These results highlight a promising approach for designing hybrid catalytic materials with hierarchical porosity, enhanced stability, and practical recyclability for environmentally relevant transformations.

1. Introduction

Nowadays, the design and development of multifunctional materials with tailored properties for diverse applications have become a major research focus in the field of materials science. In this regard, metal–organic frameworks (MOFs) have garnered significant attention over the past few decades, owing not only to their high surface areas and porosities, but also to their highly tunable pore structures and functionalities.[1–7] By carefully selecting appropriate metal ions or clusters and organic linkers, a wide variety of MOFs have been synthesized. Furthermore, the properties of MOFs can be further fine-tuned through post-synthetic modification (PSM), offering enhanced versatility. These distinctive features have positioned MOFs as promising candidates for a wide range of applications, including gas storage, drug delivery, biosensors, and catalysis.[8–16] However, many MOFs have been shown to be unstable when exposed to moisture. This instability is mainly due to the presence of metal–ligand coordination bonds, which make them more susceptible to hydrolysis compared to their inorganic counterparts, such as zeolites.[17,18] More recently, composites combining MOFs with mesoporous silica have gained increasing attention due to their hierarchical micro- and mesoporous structures.[19–22] To fabricate such composites, SBA-15 and MCM-41 featuring highly ordered channels, tunable pore sizes, and excellent thermal stability are commonly used as matrices.[23–25] The incorporation of mesoporous silica introduces additional mesopores into the composites, which facilitates diffusion and mass transfer. Moreover, the hydrothermal stability and mechanical strength of MOFs can also be significantly enhanced.[26,27] Some of the recently developed composites in this regard are MOF-5@SBA-15,[26] HKUST-1@SBA-15,[27] silica@CAT/ZIF-8,[28] Zr–MOF-808/MCM-41,[24] PMo_{12}@MOF-808@SBA-15,[29] Cu/SiO_2–MOF,[30] and ZnGlu/MOF/SBA-16.[31] However, some of the aforementioned catalytic systems suffer from catalyst leaching, separation difficulties, and poor recoverability, which limit their practical applications. Therefore, the design of integrated nanocatalysts (INCs) based on MOFs with multiple components and a hierarchically complex structure has recently attracted significant research attention, from both fundamental and industrial perspectives.

On the other hand, aromatic amines play a crucial role in the herbicide, dye, agrochemical, and pesticide industries. Furthermore, they serve as key intermediates for the synthesis of various compounds, including diazonium salts, isocyanates, azo compounds, and amides.[32–34] Sodium borohydride ($NaBH_4$) has been proposed as a promising fuel source for supplying hydride ions to reduce nitrobenzenes to their corresponding amines under mild conditions. However, $NaBH_4$ exhibits limited reducing capability in the absence of suitable additives.[35–38] Therefore, this reagent is typically employed in

Department of Chemistry, Yasouj University, Yasouj, 75918-74831, Iran. E-mail: d.elhamifar@yu.ac.ir

the presence of metallic catalysts. Another widely used and conventional approach for synthesizing aromatic amines involves the catalytic hydrogenation of the corresponding nitroarenes.[39,40] However, the homogeneous protocols for reduction of nitroarenes have different disadvantages such as separation of the catalyst and product. Therefore, it is still necessary to design effective and recoverable catalytic systems resolving these issues. A promising approach to address these limitations involves the integration of magnetic nanoparticles such as Fe_3O_4 as catalyst supports, owing to their high surface area, chemical stability, and excellent magnetic responsiveness, which enable efficient separation and reuse in heterogeneous catalytic processes.[41–44]

In view of the above, the present study aims to develop a magnetically recoverable, hierarchically porous nanocatalyst combining an Fe_3O_4 magnetic core, mesoporous MCM-41 silica, and microporous UiO-66–NH_2 MOF functionalized with a Schiff base–Pd complex. This multicomponent design addresses common challenges in catalytic systems such as catalyst separation, metal leaching, and recyclability, thereby offering a sustainable and efficient platform for the reduction of nitroarenes under mild and green conditions.

2. Experimental

2.1. Synthesis of Fe_3O_4@MCM-41

Fe_3O_4 and Fe_3O_4@SiO_2 nanoparticles were initially synthesized according to our previously reported procedures.[45,46] Subsequently, 0.6 g of Fe_3O_4@SiO_2 nanoparticles were ultrasonically dispersed in a mixture of deionized water (60 mL) and ethanol (50 mL) for 20 min. Then, 3 mL of 25% ammonia solution and 1 g of cetyltrimethylammonium bromide (CTAB) were added under continuous stirring at room temperature (RT) for 30 min. Thereafter, 0.7 mL of tetramethyl orthosilicate (TMOS) was added dropwise, and the mixture was stirred at RT for an additional 2 h. The resulting material was then statically heated under an argon atmosphere at 100 °C for 72 h. The obtained precipitate was collected using a magnet, washed with deionized water and ethanol, and dried at 65 °C for 7 h. Finally, the CTAB template was removed by calcination at 500 °C for 6 h. The final product was denoted as Fe_3O_4@MCM-41.

2.2. Synthesis of Fe_3O_4@MCM-41@UiO-66–NH_2

Initially, 1.0 g of Fe_3O_4@MCM-41 magnetic nanoparticles was fully dispersed in 50 mL of DMF under ultrasonic irradiation for 30 min. Subsequently, 0.433 g of zirconium tetrachloride, dissolved in 20 mL of DMF, was added to the reaction vessel and dispersed under ultrasonic conditions. After 20 min, 0.362 g of 2-aminoterephthalic acid (ATA), dissolved in 20 mL of DMF, was introduced into the vessel, and the reaction mixture was ultrasonicated for an additional 15 min to ensure complete dispersion. The resulting mixture was then transferred into an autoclave and heated at 120 °C for 24 h under static conditions. The synthesized material was collected using a magnet and washed several times with DMF (three times) and acetone (four times). Finally, the obtained solid was dried at 70 °C and denoted as Fe_3O_4@MCM-41@UiO-66–NH_2.

2.3. Synthesis of Fe_3O_4@MCM-41@UiO-66/SB

To achieve this, the Fe_3O_4@MCM-41@UiO-66–NH_2 nanocomposite (0.5 g) was dispersed in 30 mL of dry toluene at 25 °C for 30 min. Then, salicylaldehyde (2 mL) was added to the reaction vessel and it was allowed to reflux for 24 h. Following centrifugation, the resultant material was washed with dry EtOH and allowed to dry for 7 h at 70 °C. The solid product was denoted as Fe_3O_4@MCM-41@UiO-66/SB.

2.4. Synthesis of Fe_3O_4@MCM-41@UiO-66/SB–Pd

For this, 0.5 g of Fe_3O_4@MCM-41@UiO-66/SB was fully dispersed in 20 mL of dry EtOH at 25 °C for 30 min. Then, 1 mmol of $Pd(OAc)_2$ was added and the reaction vessel was agitated at RT for 24 h. Following centrifugation, the final product was washed with dry EtOH, dried at 70 °C for 6 h and denoted as Fe_3O_4@MCM-41@UiO-66/SB–Pd.

2.5. Procedure for the reduction of nitrobenzenes using Fe_3O_4@MCM-41@UiO-66/SB–Pd

For this purpose, 1 mmol of nitrobenzene, 2 mmol of $NaBH_4$, and 0.01 g of the Fe_3O_4@MCM-41@UiO-66/SB–Pd catalyst were added to a reaction vessel containing 10 mL of distilled water. The resulting mixture was stirred at RT and the progress of the reaction was monitored by TLC. After completion of the reaction, the catalyst was separated using a magnet. The aqueous-soluble impurities were effectively removed by decantation using a biphasic solvent system consisting of water and ethyl acetate. The resulting crude products were purified either by evaporation of the organic phase or by recrystallization from ethanol.

2.6. FT-IR and NMR data of aniline products

2.6.1. 4-Hydroxyaniline (2a). IR (KBr, cm^{-1}): 3656 (NH, stretching vibration), 3509 (OH, stretching vibration), 3046 (=C–H, stretching vibration sp^2), 1505, 1622 (C=C, Ar stretching sp^2).

2.6.2. 4-Methoxyaniline (2b). IR (KBr, cm^{-1}): 3425, 3348 (NH, stretching vibration), 3021 (=C–H, stretching vibration sp^2), 2880 (C–H, stretching vibration sp^3), 1632, 1432 (C=C, Ar stretching sp^2), 1210 (C–O, stretching vibration).

2.6.3. Benzene-1,2-diamine (2c). IR (KBr, cm^{-1}): 3583, 3453 (NH, stretching vibration), 3031 (=C–H, stretching vibration sp^2), 1516, 1617 (C=C, Ar stretching sp^2).

2.6.4. 2-Aminobenzyl alcohol (2d). IR (KBr, cm^{-1}): 3393, (NH, stretching vibration), 3142 (OH, stretching vibration), 2991 (C–H, stretching vibration sp^3), 1453, 1613 (C=C, Ar stretching sp^2).

2.6.5. 4-Bromoaniline (2e). IR (KBr, cm^{-1}): 3481, 3408 (NH, stretching vibration), 3040 (=C–H, stretching vibration sp^2), 1498, 1622 (C=C, Ar stretching sp^2). ^{1}H NMR (400 MHz, DMSO-d_6): δ (ppm) 5.29 (s, NH_2, 2H), 6.52 (d, $J = 8.8$, 2H), 7.14 (d, $J = 8.8$, 2H). ^{13}C NMR (100 MHz, DMSO-d_6): δ (ppm) 106.5, 116.2, 131.8, 148.51.

2.6.6. 4-Chloroaniline (2f). IR (KBr, cm^{-1}): 3478, 3412 (NH, stretching vibration), 3026 (=C–H, stretching vibration sp^2), 1519, 1625 (C=C, Ar stretching sp^2). ^1H NMR (400 MHz, DMSO-d_6): δ (ppm) 4.6 (s, NH_2, 2H), 6.67 (d, $J = 8.5$, 2H), 6.72 (d, $J = 8.5$, 2H). ^{13}C NMR (100 MHz, DMSO-d_6): δ (ppm) 114.9, 115.5, 142.7, 151.2.

3. Results and discussion

3.1. Characterization of Fe_3O_4@MCM-41@UiO-66/SB–Pd

Scheme 1 depicts the synthesis procedure of Fe_3O_4@MCM-41@UiO-66/SB–Pd. Fe_3O_4 and Fe_3O_4@SiO_2 NPs were first prepared according to previous methods.[47] Mesoporous silica-coated magnetic (Fe_3O_4@MCM-41) NPs were then prepared *via* the surfactant-directed condensation of TMOS over Fe_3O_4@SiO_2 NPs under basic conditions. Next, Fe_3O_4@MCM-41@UiO-66–NH_2 was solvothermally synthesized *via* chemical attachment of $ZrCl_4$/ATA based MOF on Fe_3O_4@MCM-41. Fe_3O_4@MCM-41@UiO-66–NH_2 was then chemically reacted with salicylaldehyde to afford Fe_3O_4@MCM-41@UiO-66/SB. The Fe_3O_4@MCM-41@UiO-66/SB–Pd nanocatalyst was finally obtained by treating the Fe_3O_4@MCM-41@UiO-66/SB support with $Pd(OAc)_2$.

The successful synthesis of the Fe_3O_4@MCM-41@UiO-66/SB–Pd composite was confirmed by FT-IR spectroscopy (Fig. 1). The peaks at 580 and 3409 cm^{-1} are attributed to the Fe–O and OH stretching vibrations, respectively (Fig. 1a and b).[48] Upon coating with MCM-41 silica, the additional bands at 1100 and 800 cm^{-1}, corresponding to Si–O–Si asymmetric and symmetric stretching vibrations, respectively, indicate the successful formation of MCM-41 on magnetite NPs (Fig. 1b).[49] For UiO-66–NH_2, the absorption bands at 3460 and 3351 cm^{-1} correspond to asymmetric and symmetric N–H stretching vibrations, respectively, while the band at 1660 cm^{-1} is assigned to the C=O stretching vibration of carboxylate groups. The characteristic asymmetric and symmetric stretching vibrations of

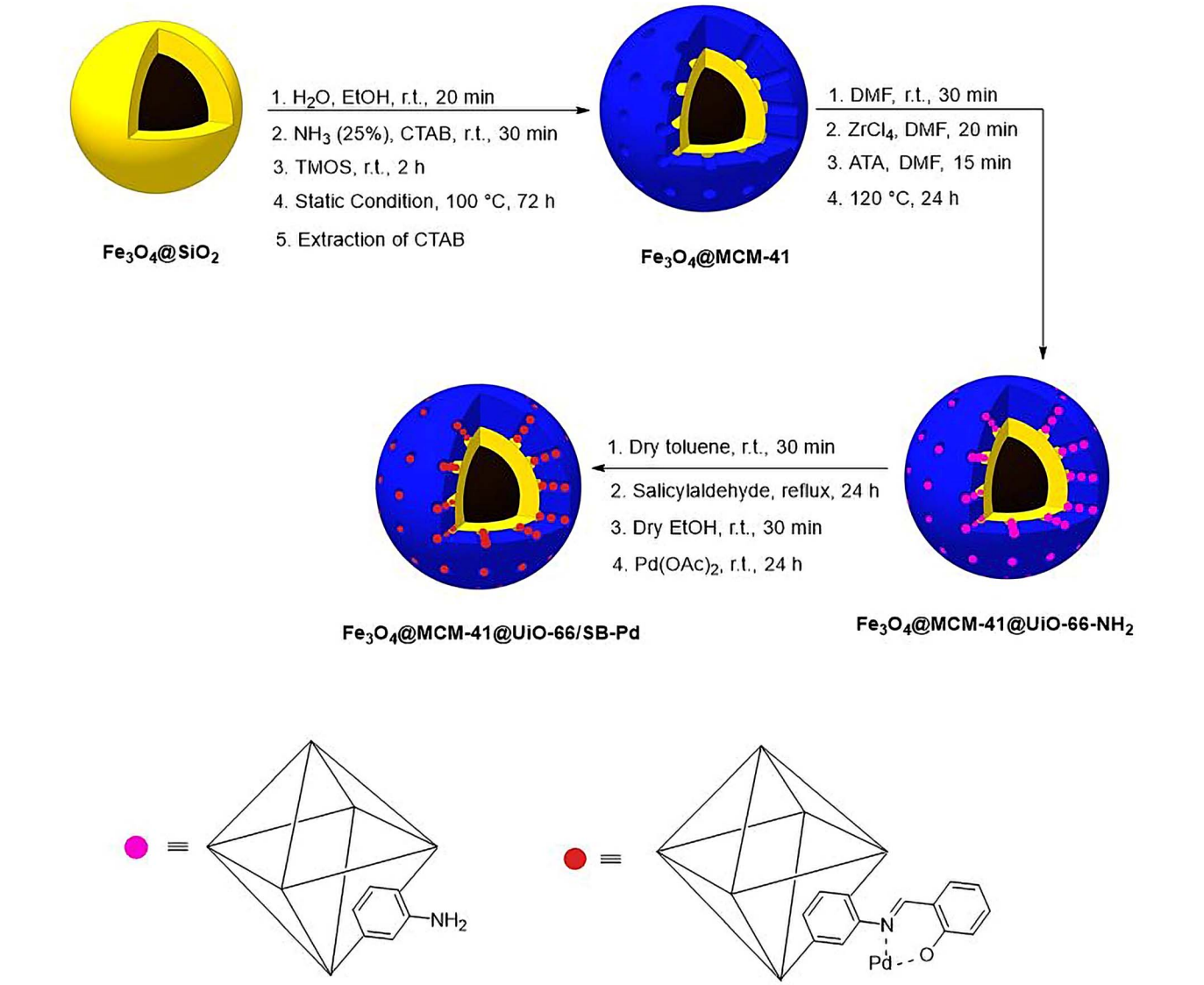

Scheme 1 Preparation of Fe_3O_4@MCM-41@UiO-66/SB–Pd.

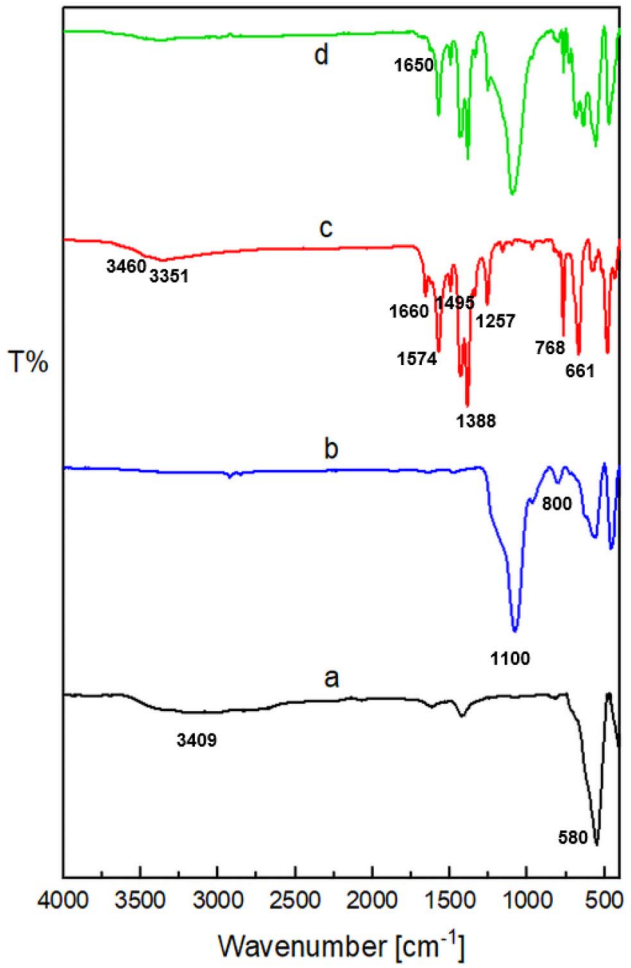

Fig. 1 FT-IR spectra of (a) Fe_3O_4, (b) Fe_3O_4@MCM-41, (c) UiO-66–NH_2, and (d) Fe_3O_4@MCM-41@UiO-66/SB–Pd.

coordinated carboxylate groups appear at 1574 and 1388 cm^{-1}, respectively. Additionally, the aromatic C=C stretching band is observed at 1495 cm^{-1}. The Zr–O stretching vibrations are also evidenced by the bands at 661 and 768 cm^{-1} (Fig. 1c).[50–52] In the final Fe_3O_4@MCM-41@UiO-66/SB–Pd composite, the retention of all characteristic bands from the core–shell structure indicates structural integrity. Notably, a new absorption band appears at 1650 cm^{-1}, which is attributed to the C=N stretching vibration of the Schiff base linkage. Additionally, the disappearance of N–H stretching bands (at 3460 and 3351 cm^{-1}) confirms the successful condensation between amine and aldehyde groups to form the imine bond (Fig. 1d).[53] These results confirm the successful construction of the designed composite.

The wide-angle powder X-ray diffraction (WAPXRD) analysis was employed to investigate the crystalline structure of the synthesized nanomaterials (Fig. 2). As illustrated, the WAPXRD pattern of Fe_3O_4@MCM-41 exhibits diffraction peaks at $2\theta \approx$ 30.3°, 35.6°, 43.2°, 53.5°, 57.1°, and 62.7°, which correspond to the (220), (311), (400), (422), (511), and (440) crystal planes of the Fe_3O_4 NPs (Fig. 2a).[54] These peaks are in good agreement with the standard JCPDS card No. 19-0629, confirming the cubic

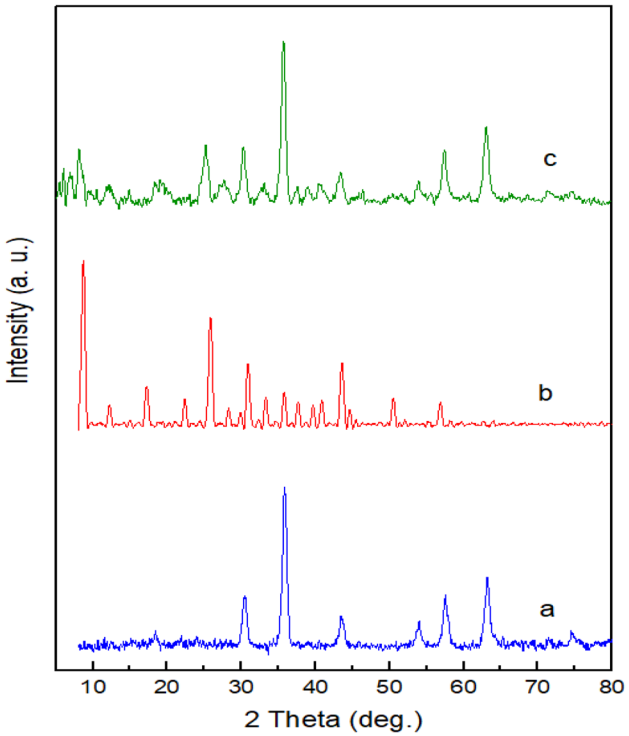

Fig. 2 WAPXRD patterns of (a) Fe_3O_4@MCM-41, (b) UiO-66–NH_2, and (c) Fe_3O_4@MCM-41@UiO-66/SB–Pd.

spinel structure of magnetite.[55,56] For UiO-66–NH_2, multiple sharp diffraction peaks observed at 2θ values of 8.6°, 14.8°, 17.3°, 22.2°, 25.9°, 30.7°, 32.1°, 35.5°, 37.7°, 40.5°, 43.3°, 50.2°, and 56.9° correspond to the crystal lattice exhibiting *Fm*3*m* symmetry of zirconium benzene carboxylate units. This indicates a highly crystalline framework of UiO-66–NH_2 (Fig. 2b).[57] The WAPXRD pattern of the final nanocomposite, Fe_3O_4@-MCM-41@UiO-66/SB–Pd (Fig. 2c), displays the characteristic

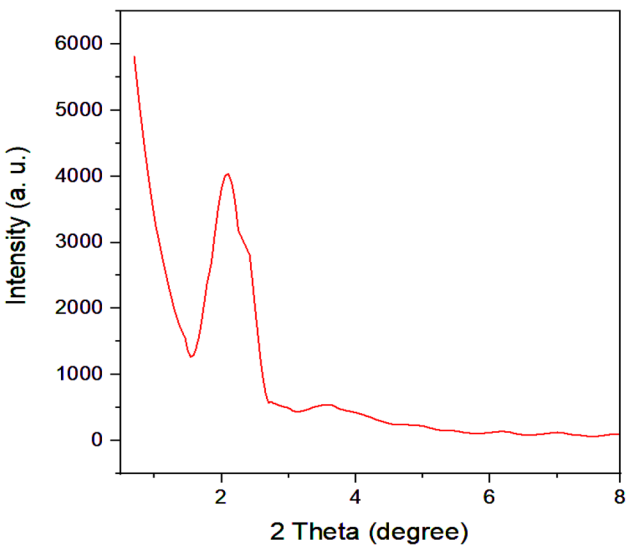

Fig. 3 Low-angle PXRD pattern of Fe_3O_4@MCM-41@UiO-66/SB–Pd.

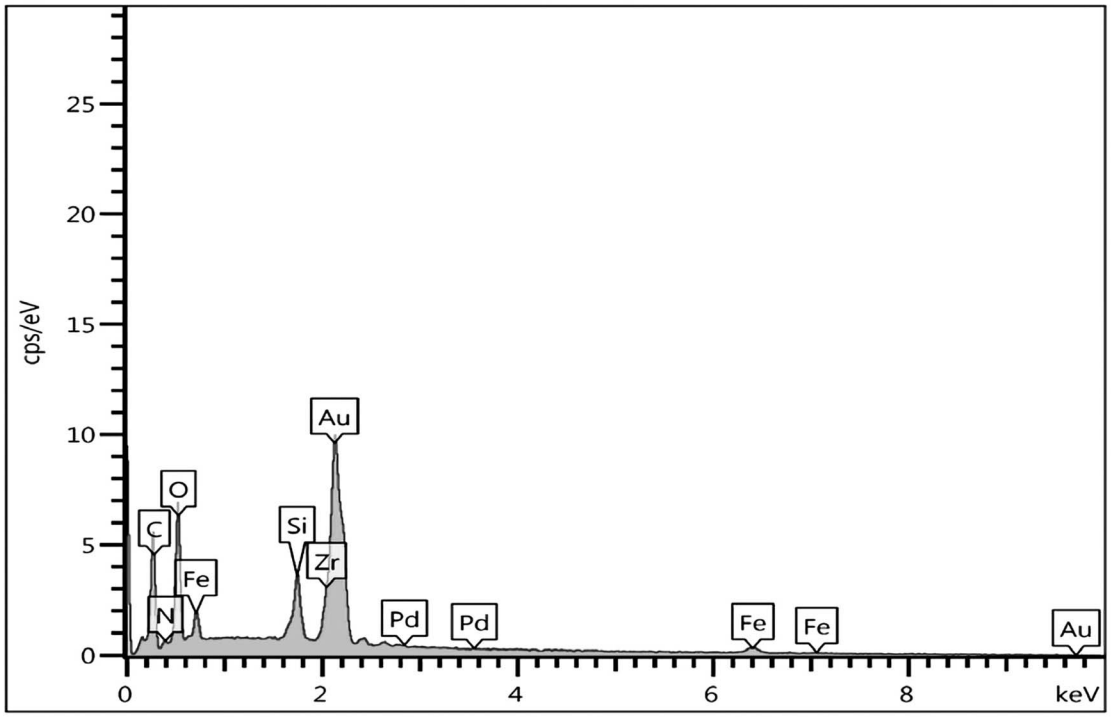

Fig. 4 EDX spectrum of Fe_3O_4@MCM-41@UiO-66/SB–Pd.

diffraction peaks of both Fe_3O_4 and UiO-66–NH_2, confirming the successful synthesis of the hybrid material. Moreover, the observed reduction in peak intensity in the final nanocomposite can be attributed to the incorporation of UiO-66–NH_2 into the magnetic MCM-41 framework.

The low-angle PXRD pattern of Fe_3O_4@MCM-41@UiO-66/SB–Pd displays a distinct diffraction peak at $2\theta \approx 2.2°$ (Fig. 3), corresponding to the (100) reflection of the ordered hexagonal mesophase of MCM-41. This result confirms that the mesoporous structure of MCM-41 is well preserved after the successive functionalization and MOF incorporation steps.

The energy-dispersive X-ray (EDX) analysis was also carried out to investigate the existence of expected elements. As depicted, the signals of Fe, O, Si, C, N, Zr, and Pd prove successful synthesis of the designed material (Fig. 4).

Moreover, the EDX-mapping analysis clearly demonstrated the uniform distribution of the aforementioned elements in the Fe_3O_4@MCM-41@UiO-66/SB–Pd framework (Fig. 5).

Thermal stability and composition of Fe_3O_4@MCM-41@UiO-66/SB–Pd were examined using TG analysis. As presented in Fig. 6, the TG curve demonstrates four weight loss steps. The first stage below 150 °C is caused by the removal of physically adsorbed water, indicating a moisture content of about 5% in the sample. The second weight loss (~10%) between 170 and 230 °C corresponds to the thermal decomposition of the remaining CTAB surfactant. A significant weight

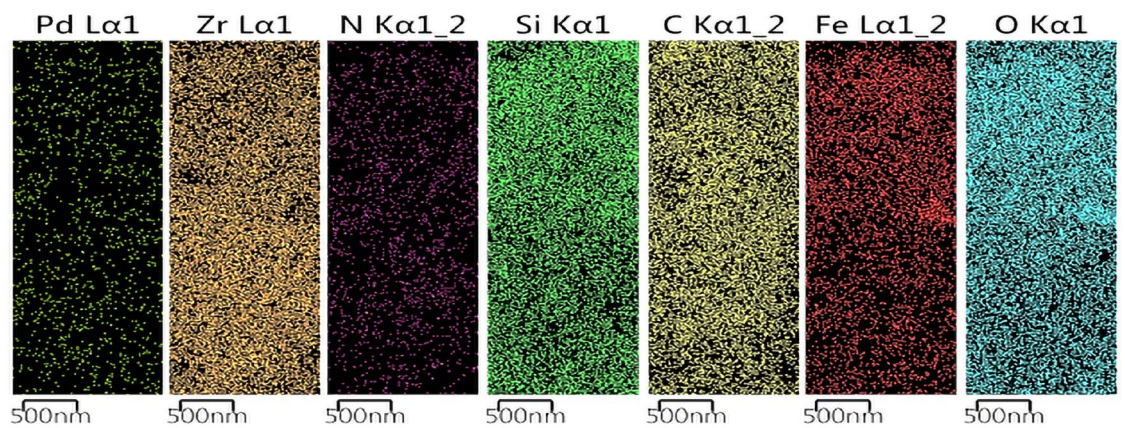

Fig. 5 EDX-mapping of Fe_3O_4@MCM-41@UiO-66/SB–Pd.

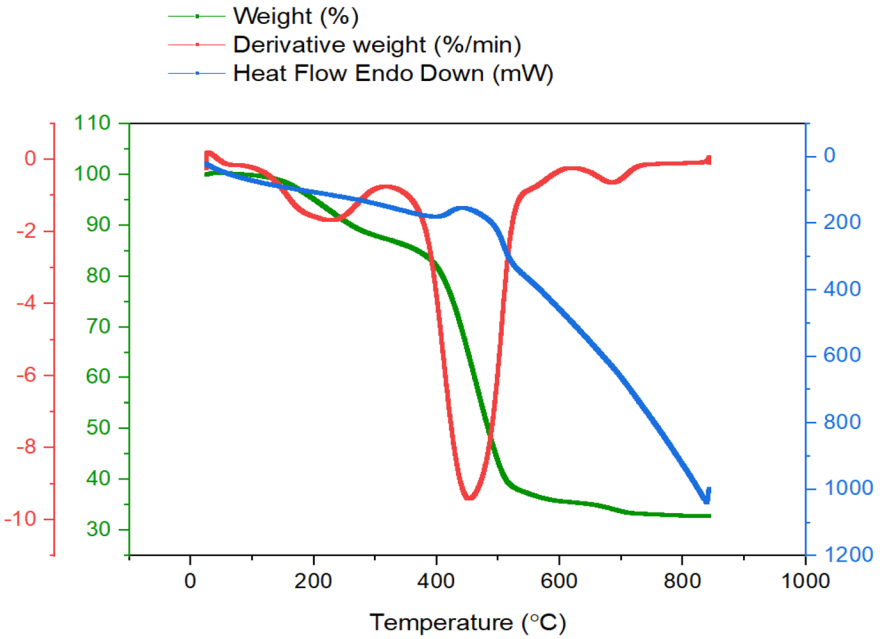

Fig. 6 TG curve of Fe_3O_4@MCM-41@UiO-66/SB–Pd.

loss (~50%) occurs between 235 and 700 °C due to degradation of Schiff-base moieties and organic ligands of the UiO-66 framework and also combustion of residual carbon.[58,59] These findings confirm the thermal robustness of the designed composite.

The morphology of Fe_3O_4@MCM-41, UiO-66–NH_2 and Fe_3O_4@MCM-41@UiO-66/SB–Pd was studied using SEM, as shown in Fig. 6. Analysis of the images revealed that Fe_3O_4@MCM-41 NPs have good spherical morphology with uniform particle size (Fig. 7a). This also showed that UiO-66–NH_2 crystallized in

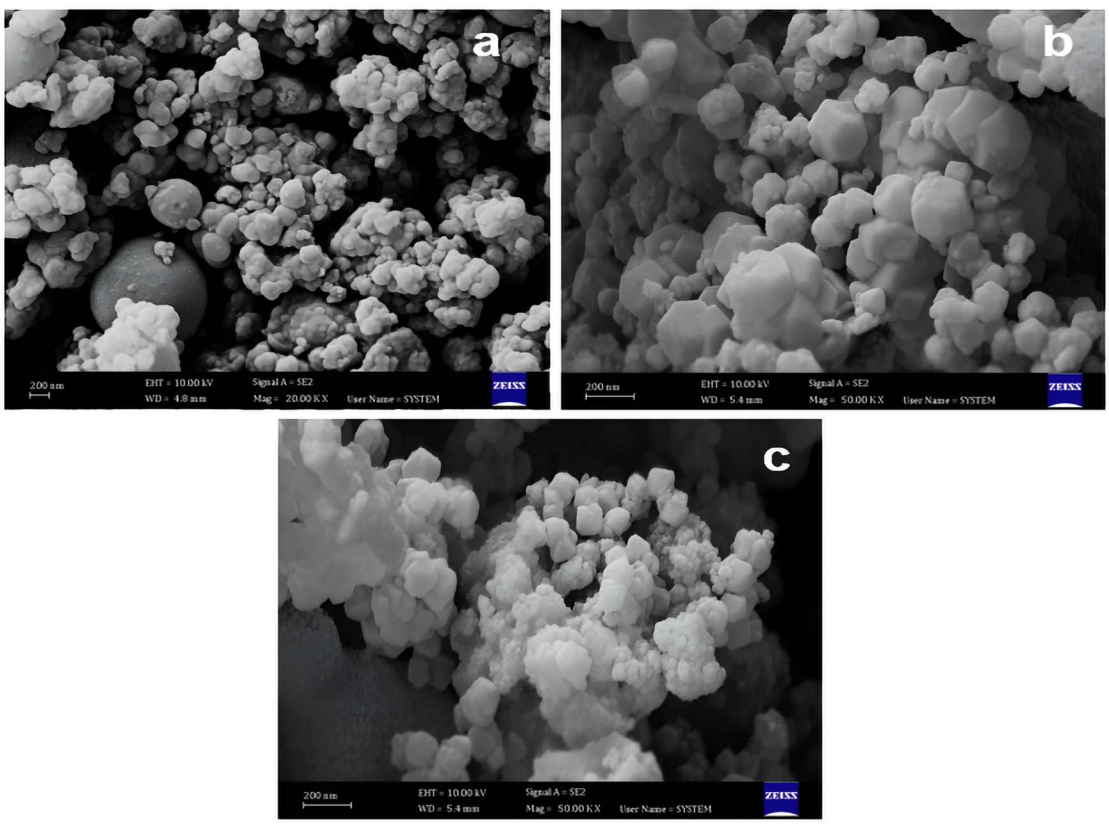

Fig. 7 SEM images of (a) Fe_3O_4@MCM-41, (b) UiO-66–NH_2, and (c) Fe_3O_4@MCM-41@UiO-66/SB–Pd.

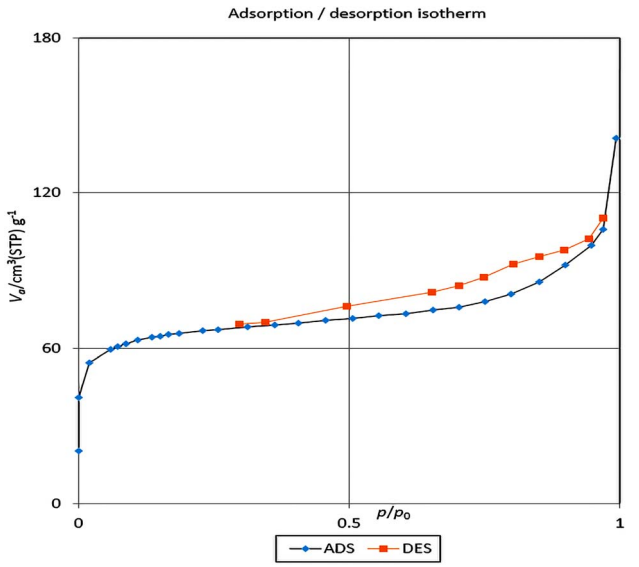

Fig. 8 N_2 adsorption–desorption isotherms of Fe_3O_4@MCM-41@UiO-66/SB–Pd.

well-defined octahedral structures with smooth surfaces and uniform size distribution (Fig. 7b). Upon formation of the final composite, Fe_3O_4@MCM-41@UiO-66/SB–Pd (Fig. 7c), a noticeable change in morphology is observed. The particles become more irregular with a complex surface topology resulting from surface functionalization, confirming the effective immobilization of UiO-66–NH_2 within the magnetic MCM-41 nanocomposite.

The specific surface area and porosity of Fe_3O_4@MCM-41@UiO-66/SB–Pd were investigated using nitrogen adsorption–desorption measurements at 77 K. As shown in Fig. 8, the isotherm displays a typical type IV profile with an H1-type hysteresis loop, which is characteristic of mesoporous materials and can be attributed to the presence of MCM-41. Additionally, the sharp uptake at low relative pressures indicates the existence of micropores, likely originating from the UiO-66–NH_2 framework. The composite exhibits a high specific surface area of 249.1 $m^2\ g^{-1}$ and an average pore diameter of 1.2 nm. This combination of micro- and mesoporosity, along with the large surface area, renders the material highly suitable for catalytic and adsorption applications.

The magnetic properties of materials were investigated using a vibrating sample magnetometer (VSM) (Fig. 9). The saturated magnetization values of Fe_3O_4@SiO_2 (Fig. 9a), Fe_3O_4@MCM-41 (Fig. 9b) and Fe_3O_4@MCM-41@UiO-66/SB–Pd (Fig. 9c) were found to be 56, 40 and 20 emu g^{-1}, respectively. This gradual reduction in magnetic saturation is attributed to the well coating of the MCM-41 shell and UiO-66–NH_2 around Fe_3O_4 NPs.

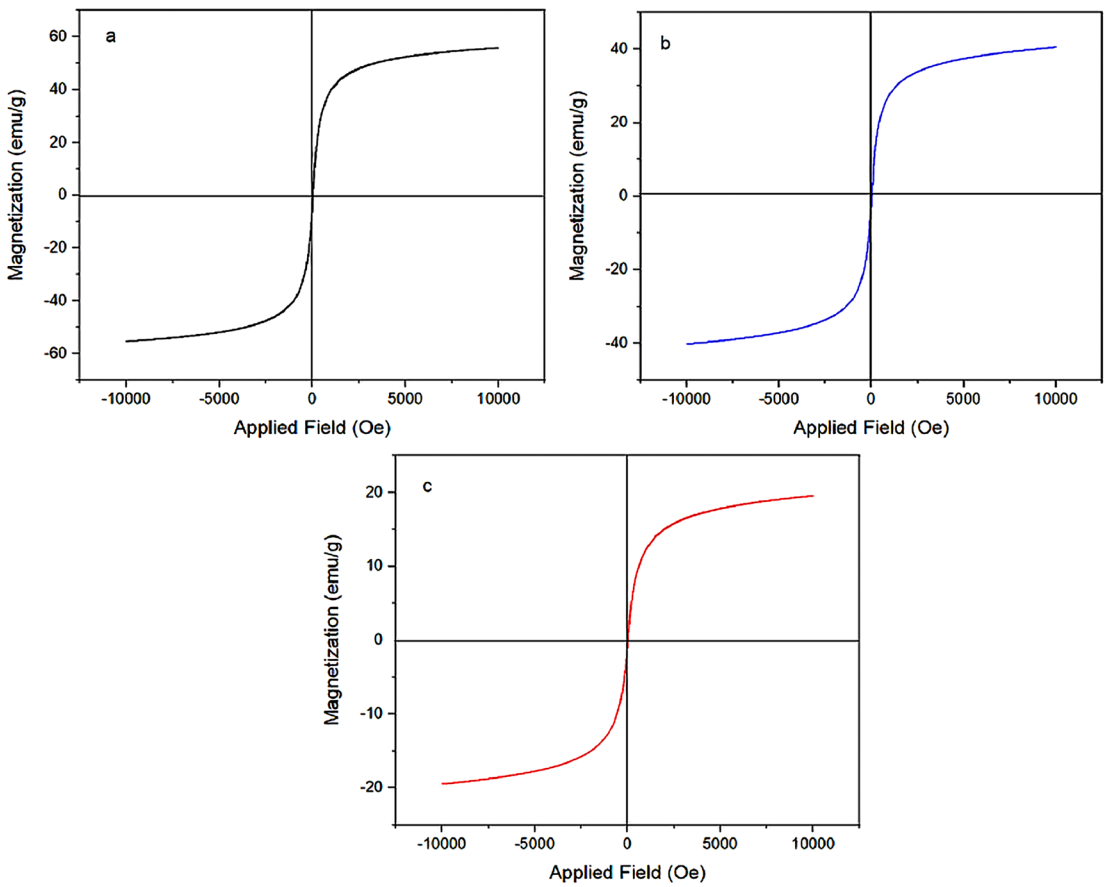

Fig. 9 VSM curves of (a) Fe_3O_4@SiO_2, (b) Fe_3O_4@MCM-41 and (c) Fe_3O_4@MCM-41@UiO-66/SB–Pd.

Table 1 Effect of catalyst loading and solvent on the reduction of 4-nitrophenol

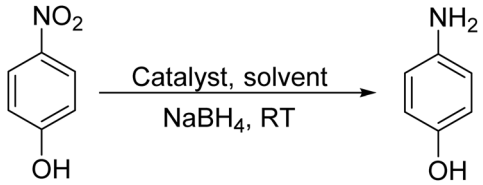

Entry	Catalyst	Catalyst amount (g)	Solvent	Time (min)	Yield[a] (%)
1	—	—	H_2O	60	—
2	Fe_3O_4@MCM-41@UiO-66/SB–Pd	0.005	H_2O	30	81
3[b]	Fe_3O_4@MCM-41@UiO-66/SB–Pd	0.01	H_2O	30	95
4	Fe_3O_4@MCM-41@UiO-66/SB–Pd	0.015	H_2O	30	96
5	Fe_3O_4@MCM-41@UiO-66/SB–Pd	0.01	MeOH	30	78
6	Fe_3O_4@MCM-41@UiO-66/SB–Pd	0.01	EtOH	30	59
7	Fe_3O_4@MCM-41@UiO-66/SB–Pd	0.01	THF	30	43
8	Fe_3O_4@MCM-41@UiO-66/SB–Pd	0.01	DMF	30	31
9	Fe_3O_4@MCM-41@UiO-66/SB	0.01	H_2O	30	—
10	Fe_3O_4@MCM-41@UiO-66–NH_2	0.01	H_2O	30	—
11	Fe_3O_4@MCM-41	0.01	H_2O	30	—

[a] Isolated yield. [b] Optimized conditions.

3.2. Catalytic performance

After the comprehensive characterization of Fe_3O_4@MCM-41@UiO-66/SB–Pd, its performance was studied in the reduction of nitroarenes in the presence of $NaBH_4$ at room temperature (RT). The effect of different parameters was studied in the reduction of 4-nitrophenol as a reaction model (Table 1). As shown, in the absence of the catalyst, along with 2 mmol of $NaBH_4$, no reduction was observed (Table 1, entry 1). To determine the optimal amount of the catalyst, a model reaction was carried out using different catalyst loadings (Table 1, entries 2–4). The results indicated that the highest yield is obtained in the presence of 0.01 g of Fe_3O_4@MCM-41@UiO-66/SB–Pd. Notably, increasing the catalyst loading beyond this amount did not result in a significant improvement in reaction progress (Table 1, entry 3 *vs.* entry 4). Subsequently, to investigate the effect of the solvent, the model reaction was conducted in various solvents including H_2O, EtOH, MeOH, THF, and DMF. The results revealed that the reaction proceeded more efficiently in polar protic solvents, and H_2O was selected as a green solvent (Table 1, entry 3 *vs.* entries 5–8). In another experiment, the role of palladium species was evaluated by conducting the model reaction in the presence of Pd-free Fe_3O_4@MCM-41, Fe_3O_4@MCM-41@UiO-66–NH_2, and Fe_3O_4@MCM-41@UiO-66/SB nanocomposites. The obtained results revealed that no product is formed in the absence of palladium, indicating the key role of Pd species as active catalytic centers (Table 1, entry 3 *vs.* entries 9–11). Therefore, the optimal reaction conditions for the reduction of nitrobenzenes were identified as using 0.01 g of Fe_3O_4@MCM-41@UiO-66/SB–Pd in water at RT (Table 1, entry 3).

Table 2 Reduction of nitrobenzenes using Fe_3O_4@MCM-41@UiO-66/SB–Pd

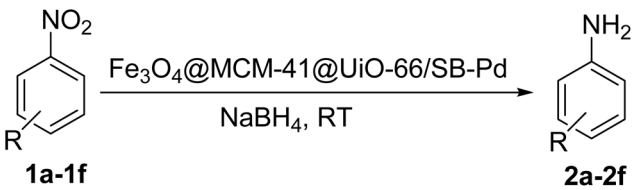

Entry	R	Time (min)	Product	Yield (%)	M.P. (°C)	Reported M.P. (°C) (ref.)
1	4-OH	30	**2a**	95	184–186	185–186 (ref. 60)
2	4-MeO	27	**2b**	90	57–59	59–61 (ref. 60)
3	2-NH_2	27	**2c**	88	104–106	106–108 (ref. 60)
4	2-CH_2OH	30	**2d**	86	80–82	80–82 (ref. 60)
5	4-Br	25	**2e**	93	63–65	60–63 (ref. 60)
6	4-Cl	23	**2f**	96	68–70	70–72 (ref. 46)

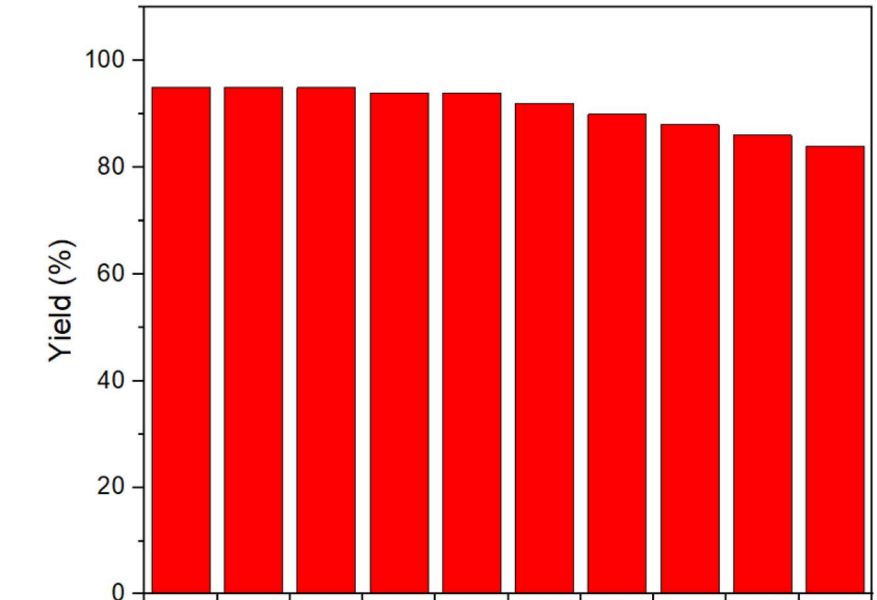

	1	2	3	4	5	6	7	8	9	10
Time (min)	30	30	35	35	40	45	50	60	75	90
Yield (%)	95	95	95	94	94	92	90	88	86	84

Fig. 10 Recoverability and reusability of Fe_3O_4@MCM-41@UiO-66/SB–Pd.

After optimizing the reaction conditions, a wide range of nitroaromatic derivatives were examined in the reduction reaction (Table 2). The results revealed that all nitroaromatic compounds bearing either electron-withdrawing or electron-donating substituents are efficiently converted into the corresponding amines in excellent yields using the Fe_3O_4@-MCM-41@UiO-66/SB–Pd catalyst. These findings highlight the high catalytic activity and selectivity of the designed nano-composite in this process.

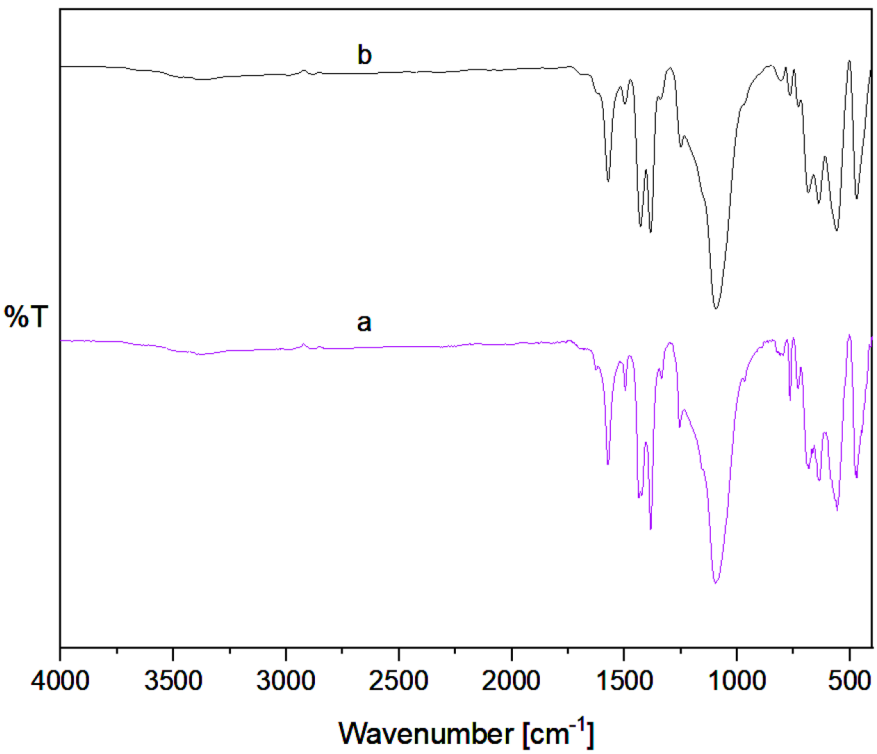

Fig. 11 FTIR spectra of (a) fresh and (b) recovered Fe_3O_4@MCM-41@UiO-66/SB–Pd catalyst.

Table 3 Comparative study of the efficiency of Fe_3O_4@MCM-41@UiO-66/SB–Pd with that of former catalysts in the reduction of nitrobenzenes

Entry	Catalyst	Reaction conditions	Recovery times	Ref.
1	Pd@A-ZIF-67	H_2O : EtOH (1 : 1), $NaBH_4$, RT, catalyst (0.05 mol%)	6	61
2	SiO_2@β-CD@Pd-PDR	H_2O, $NaBH_4$, RT, catalyst (20 mg)	10	62
3	Pd@CQD@Fe_3O_4	H_2O : EtOH (5 : 1), $NaBH_4$, RT, catalyst (0.008 mol%)	7	63
4	Co@NC	H_2O, $NaBH_4$, RT, catalyst (8 mg)	6	64
5	Fe_3O_4/PVA-10% Ag	EtOH, $N_2H_4 \cdot H_2O$, 70 °C, catalyst (30 mg)	5	65
6	Pd–NHC–γ-Fe_2O_3–*n*-butyl-SO_3H	H_2O, $NaBH_4$, RT, catalyst (0.6 mol%)	6	66
7	Fe_3O_4@MCM-4@UiO-66/SB–Pd	H_2O, $NaBH_4$, RT, catalyst (0.01 g)	9	This work

Considering the importance of the stability of the catalyst for its practical applications, in the next study, the recyclability of the Fe_3O_4@MCM-41@UiO-66/SB–Pd catalyst was evaluated in the model reaction. For this, upon reaction completion, the catalyst was efficiently recovered using an external magnet, thoroughly washed with EtOH, and dried prior to reuse in subsequent cycles. As illustrated in Fig. 10, the catalyst retained its catalytic activity over nine consecutive runs with negligible loss in performance. These findings confirm the effective immobilization and high stability of Pd species on the support throughout the reaction cycles.

The structural stability of the Fe_3O_4@MCM-41@UiO-66/SB–Pd catalyst after recycling was evaluated using FT-IR spectroscopy. As shown in Fig. 11, the FT-IR spectra of the fresh and reused catalyst after the nine reaction cycles have the same pattern with no noticeable change in the characteristic absorption bands. This observation confirms that the catalyst retained its structural integrity upon repeated use, highlighting its excellent chemical stability and reusability.

Furthermore, the stability and heterogeneous nature of the Fe_3O_4@MCM-41@UiO-66/SB–Pd catalyst were evaluated through a leaching test. In this procedure, the catalyst was magnetically separated from the reaction mixture upon reaching approximately 50% conversion. The resulting residue was then stirred under identical reaction conditions for an additional 60 min. Interestingly, no appreciable increase in product formation was observed, indicating the absence of active Pd species in the solution and confirming the truly heterogeneous character of the catalyst.

In the next study, the performance of Fe_3O_4@MCM-41@UiO-66/SB–Pd was compared to that of other previously reported catalytic systems used in the reduction of nitroarene reaction (Table 3). The results revealed that the present catalyst provides significant advantages regarding reaction temperature, catalyst loading, and recyclability. These outcomes highlight the high efficiency, stability, and durability of the designed catalyst.

4. Conclusion

In summary, a multifunctional composite, Fe_3O_4@MCM-41@UiO-66/SB–Pd, was successfully fabricated through a stepwise surface functionalization strategy. MCM-41 served as a structural bridge, enabling uniform integration of UiO-66–NH_2 nanocrystals and Schiff base–Pd complexes while maintaining magnetic properties of Fe_3O_4 NPs. The resulting catalyst combined the high surface area and accessible pore architecture of both mesoporous and microporous components with the catalytic functionality of Pd active sites. Comprehensive physicochemical characterization confirmed the retention of crystallinity, hierarchical porosity, thermal stability, and superparamagnetic behavior throughout the synthesis. Owing to these features, the composite demonstrated efficient catalytic performance in the reduction of nitroarenes under mild conditions, along with excellent magnetic recoverability and reusability. Importantly, the high reusability of the catalyst combined with simple magnetic separation reduces the overall operational cost, making it a cost effective alternative to conventional homogeneous and heterogeneous catalytic systems. These findings demonstrate the potential of such hybrid composites for environmentally benign catalytic applications and offer a promising platform for future multifunctional material design.

Conflicts of interest

There are no conflicts to declare.

Data availability

The data supporting this article have been included as part of the supplementary information (SI). Supplementary information: raw data of performed analyses. See DOI: **https://doi.org/10.1039/d5na00543d**.

Acknowledgements

The authors acknowledge Yasouj University and the Iran National Science Foundation (INSF) for supporting this work.

References

1 C. Liu, J. Wang, J. Wan and C. Yu, MOF-on-MOF hybrids: synthesis and applications, *Coord. Chem. Rev.*, 2021, **432**, 213743.
2 J. Fonseca, T. Gong, L. Jiao and H.-L. Jiang, Metal–organic frameworks (MOFs) beyond crystallinity: amorphous MOFs, MOF liquids and MOF glasses, *J. Mater. Chem. A*, 2021, **9**, 10562–10611.
3 I. E. Khalil, J. Fonseca, M. R. Reithofer, T. Eder and J. M. Chin, Tackling orientation of metal-organic

frameworks (MOFs): the quest to enhance MOF performance, *Coord. Chem. Rev.*, 2023, **481**, 215043.
4 G. Cai, P. Yan, L. Zhang, H.-C. Zhou and H.-L. Jiang, Metal–Organic Framework-Based Hierarchically Porous Materials: Synthesis and Applications, *Chem. Rev.*, 2021, **121**, 12278–12326.
5 A. Ghosh, S. Bhattacharjee, S. Chongdar, T. Sen, S. Banerjee, A. K. Das and A. Bhaumik, Tandem cooperative catalysis over a Zr-MOF for the synthesis of hydroxyurethanes under solvent-free conditions, *Appl. Catal., A*, 2025, **704**, 120397.
6 A. Kaur, Y. Singh, A. Singh, S. Kaushal and R. Badru, Efficient and selective N-benzylation of amines using Pd-doped La-BDC MOF, *Mater. Adv.*, 2025, **6**, 5196–5209.
7 M. Kaur, A. Sharma, Y. Singh, A. Singh, H. Kaur, S. Kumar, S. Kaushal and R. Badru, Pd supported Al-BDC MOF for efficient and selective N-methylation of amines under solventless conditions, *Emergent Mater.*, 2024, **7**, 1683–1693.
8 D. H. Hong, H. S. Shim, J. Ha and H. R. Moon, MOF-on-MOF architectures: applications in separation, catalysis, and sensing, *Bull. Korean Chem. Soc.*, 2021, **42**, 956–969.
9 X. Zhang, F. Peng and D. Wang, MOFs and MOF-derived materials for antibacterial application, *J. Funct. Biomater.*, 2022, **13**, 215.
10 S. Mallakpour, E. Nikkhoo and C. M. Hussain, Application of MOF materials as drug delivery systems for cancer therapy and dermal treatment, *Coord. Chem. Rev.*, 2022, **451**, 214262.
11 R. Freund, O. Zaremba, G. Arnauts, R. Ameloot, G. Skorupskii, M. Dincă, A. Bavykina, J. Gascon, A. Ejsmont and J. Goscianska, The current status of MOF and COF applications, *Angew. Chem., Int. Ed.*, 2021, **60**, 23975–24001.
12 Y. M. Jo, Y. K. Jo, J. H. Lee, H. W. Jang, I. S. Hwang and D. J. Yoo, MOF-based chemiresistive gas sensors: toward new functionalities, *Adv. Mater.*, 2023, **35**, 2206842.
13 B. Mohanty, S. Kumari, P. Yadav, P. Kanoo and A. Chakraborty, Metal-organic frameworks (MOFs) and MOF composites based biosensors, *Coord. Chem. Rev.*, 2024, **519**, 216102.
14 A. Sharma, S. Bedi, K. Verma, B. Lal, V. John, R. Kumar, S. Kaushal and R. Badru, Ce-Zr UiO-66 MOF as recyclable heterogeneous catalyst for selective N-methylation, *Polyhedron*, 2023, **242**, 116517.
15 A. Sharma, K. Verma, S. Kaushal and R. Badru, A novel 2-D accordion like Al-BPED MOF as reusable and selective catalyst for N-alkylation of amines with dialkylcarbonates, *Appl. Organomet. Chem.*, 2022, **36**, e6814.
16 M. Sharma, A. Singh, S. Kaushal and R. Badru, Zinc Fumarate MOF: An Efficient and Facile Catalyst for Biginelli Reaction, *Appl. Organomet. Chem.*, 2025, **39**, e70086.
17 M. Ding, X. Cai and H.-L. Jiang, Improving MOF stability: approaches and applications, *Chem. Sci.*, 2019, **10**, 10209–10230.
18 B. Liu, K. Vikrant, K.-H. Kim, V. Kumar and S. K. Kailasa, Critical role of water stability in metal–organic frameworks and advanced modification strategies for the extension of their applicability, *Environ. Sci.: Nano*, 2020, **7**, 1319–1347.
19 Z. Hua, S. Cai, H. Xu, W. Yuan, S. Li and Z. Tu, Investigations of Silica/MOF composite coating and its dehumidification performance on a desiccant-coated heat exchanger, *Energy*, 2024, **307**, 132576.
20 Y. Zhou, J. Wang, J. Yang, L.-H. Duan, H.-B. Liu, J. Wu and L. Gao, Mesoporous silica-confined MOF-525 for stable adsorption of tetracycline over a wide pH application range, *ACS Appl. Nano Mater.*, 2024, **7**, 3806–3816.
21 S. E. Massimi, K. E. Metzger, C. M. McGuirk and B. G. Trewyn, Best Practices in the Characterization of MOF@MSN Composites, *Inorg. Chem.*, 2022, **61**, 4219–4234.
22 L. Ge, Y. Feng, Y. Xue, Y. Dai, R. Wang and T. Ge, Mesoporous Silica-Guided Synthesis of Metal–Organic Framework with Enhanced Water Adsorption Capacity for Smart Indoor Humidity Regulation, *Small Struct.*, 2023, **4**, 2300055.
23 E. García-Rojas, J. Tapiador, P. Leo, C. Martos and G. Orcajo, Synergistic performance of novel Cu-MOF-74@SBA-15 material in enhanced CO_2 adsorption and transformation, *J. CO_2 Util.*, 2025, **92**, 103025.
24 G. Morales, M. Paniagua, D. de la Flor, M. Sanz, P. Leo, C. López-Aguado, H. Hernando, S. A. Orr, K. Wilson, A. F. Lee and J. A. Melero, Aldol condensation of furfural and methyl isobutyl ketone over Zr-MOF-808/silica hybrid catalysts, *Fuel*, 2023, **339**, 127465.
25 S. Dalakoti, N. Singh, A. Sharma, A. Singh, M. Sachdeva, S. Divekar, A. Arya, R. S. Murali and S. Dasgupta, Cu-trimesate and mesoporous silica composite as adsorbent showing enhanced CO_2/CH_4 and CO_2/N_2 selectivity for biogas and flue gas separation, *Microporous Mesoporous Mater.*, 2025, **381**, 113354.
26 J. Kou and L.-B. Sun, Fabrication of Metal–Organic Frameworks inside Silica Nanopores with Significantly Enhanced Hydrostability and Catalytic Activity, *ACS Appl. Mater. Interfaces*, 2018, **10**, 12051–12059.
27 C. Chen, B. Li, L. Zhou, Z. Xia, N. Feng, J. Ding, L. Wang, H. Wan and G. Guan, Synthesis of Hierarchically Structured Hybrid Materials by Controlled Self-Assembly of Metal–Organic Framework with Mesoporous Silica for CO_2 Adsorption, *ACS Appl. Mater. Interfaces*, 2017, **9**, 23060–23071.
28 J. Cui, Y. Feng and S. Jia, Silica encapsulated catalase@metal-organic framework composite: a highly stable and recyclable biocatalyst, *Chem. Eng. J.*, 2018, **351**, 506–514.
29 S. C. Fernandes, P. Leo, I. Santos-Vieira, B. de Castro, L. Cunha-Silva and S. S. Balula, Improving Oxidative Catalytic Efficiency for Fuels Desulfurization Using Hybrid Materials Based in MOF-808@SBA-15, *ChemCatChem*, 2024, **16**, e202400355.
30 R.-P. Ye, L. Lin, C.-C. Chen, J.-X. Yang, F. Li, X. Zhang, D.-J. Li, Y.-Y. Qin, Z. Zhou and Y.-G. Yao, Synthesis of Robust MOF-Derived Cu/SiO_2 Catalyst with Low Copper Loading via Sol–Gel Method for the Dimethyl Oxalate Hydrogenation Reaction, *ACS Catal.*, 2018, **8**, 3382–3394.
31 H. Torabi, H. Eshghi, S. S. E. Ghodsinia and P. Sanati-Tirgan, Design and synthesis of ZnGlu MOF/SBA-16 nanocomposite,

and its performance as an environmentally friendly nanocomposite for solvent-free chemical fixation of CO_2 to epoxides for high-yield synthesis of cyclic carbonates, *Mol. Catal.*, 2023, **550**, 113552.

32 D. Formenti, F. Ferretti, F. K. Scharnagl and M. Beller, Reduction of nitro compounds using 3D-non-noble metal catalysts, *Chem. Rev.*, 2018, **119**, 2611–2680.

33 M. Nasrollahzadeh, Z. Nezafat, M. G. Gorab and M. Sajjadi, Recent progresses in graphene-based (photo) catalysts for reduction of nitro compounds, *Mol. Catal.*, 2020, **484**, 110758.

34 H. Goksu, H. Sert, B. Kilbas and F. Sen, Recent advances in the reduction of nitro compounds by heterogenous catalysts, *Curr. Org. Chem.*, 2017, **21**, 794–820.

35 N. Zengin, H. Göksu and F. Şen, Chemoselective hydrogenation of aromatic nitro compounds in the presence of homogeneous Pd based catalysts, *Chemosphere*, 2021, **282**, 130887.

36 K. Zhang, J. M. Suh, J.-W. Choi, H. W. Jang, M. Shokouhimehr and R. S. Varma, Recent Advances in the Nanocatalyst-Assisted $NaBH_4$ Reduction of Nitroaromatics in Water, *ACS Omega*, 2019, **4**, 483–495.

37 S. Fountoulaki, V. Daikopoulou, P. L. Gkizis, I. Tamiolakis, G. S. Armatas and I. N. Lykakis, Mechanistic Studies of the Reduction of Nitroarenes by $NaBH_4$ or Hydrosilanes Catalyzed by Supported Gold Nanoparticles, *ACS Catal.*, 2014, **4**, 3504–3511.

38 S. K. Das, R. Chatterjee and A. Bhaumik, Ultrasmall Bismuth Nanoparticles Supported over Nitrogen-Rich Porous Triazine-Piperazine Polymer for Efficient Catalytic Reduction, *Chem.–Asian J.*, 2025, **20**, e202401302.

39 K. Murugesan, Z. Wei, V. G. Chandrashekhar, H. Jiao, M. Beller and R. V. Jagadeesh, General and selective synthesis of primary amines using Ni-based homogeneous catalysts, *Chem. Sci.*, 2020, **11**, 4332–4339.

40 C. Dewangan, S. Kumawat, T. Bhatt and K. Natte, Homogenous nickel-catalyzed chemoselective transfer hydrogenation of functionalized nitroarenes with ammonia–borane, *Chem. Commun.*, 2023, **59**, 14709–14712.

41 J. Mondal, K. T. Nguyen, A. Jana, K. Kurniawan, P. Borah, Y. Zhao and A. Bhaumik, Efficient alkene hydrogenation over a magnetically recoverable and recyclable Fe_3O_4@GO nanocatalyst using hydrazine hydrate as the hydrogen source, *Chem. Commun.*, 2014, **50**, 12095–12097.

42 S. Payamifar, A. Foroozandeh, M. Abdouss and A. Poursattar Marjani, Magnetic nickel nanoparticle catalyst on β-cyclodextrin-modified Fe_3O_4 for nitroarene hydrogenation, *Sci. Rep.*, 2024, **14**, 28493.

43 A. M. Antony, V. Kandathil, M. Kempasiddaiah, R. B. Dateer and S. A. Patil, Magnetic nanoparticles embedded hexagonal boron nitride tethered N-heterocyclic carbene-palladium(II): an efficient and reusable magnetic catalyst for fluoride-free Hiyama cross-coupling and 4-nitrophenol reduction reactions, *J. Phys. Chem. Solids*, 2023, **177**, 111283.

44 S. Roy, D. K. Mondal, S. Chatterjee, A. Chowdhury, T. S. Khan, M. A. Haider, S. Mandal, D. Chandra, M. Hara and A. Bhaumik, Selective CO_2 reduction to methane catalyzed by mesoporous Ru-Fe_3O_4/CeO_x-SiO_2 in a fixed bed flow reactor, *Mol. Catal.*, 2022, **528**, 112486.

45 M. Neysi, A. Zarnegaryan and D. Elhamifar, Core–shell structured magnetic silica supported propylamine/molybdate complexes: an efficient and magnetically recoverable nanocatalyst, *New J. Chem.*, 2019, **43**, 12283–12291.

46 R. Mirbagheri and D. Elhamifar, Magnetic ethyl-based organosilica supported Schiff-base/indium: a very efficient and highly durable nanocatalyst, *J. Alloys Compd.*, 2019, **790**, 783–791.

47 M. Norouzi, D. Elhamifar and S. Kargar, Magnetic yolk-shell structured periodic mesoporous organosilica supported palladium as a powerful and highly recoverable nanocatalyst for the reduction of nitrobenzenes, *Sci. Rep.*, 2024, **14**, 16262.

48 S. Kargar, D. Elhamifar and A. Zarnegaryan, Core–shell structured Fe_3O_4@SiO_2-supported IL/$[Mo_6O_{19}]$: a novel and magnetically recoverable nanocatalyst for the preparation of biologically active dihydropyrimidinones, *J. Phys. Chem. Solids*, 2020, **146**, 109601.

49 F. Mousavi, D. Elhamifar and S. Kargar, Copper/IL-containing magnetic nanoporous MCM-41: a powerful and highly stable nanocatalyst, *Surf. Interfaces*, 2021, **25**, 101225.

50 K. Wang, J. Gu and N. Yin, Efficient removal of Pb(II) and Cd(II) using NH_2-functionalized Zr-MOFs via rapid microwave-promoted synthesis, *Ind. Eng. Chem. Res.*, 2017, **56**, 1880–1887.

51 F. Zhang, S. Zheng, Q. Xiao, Y. Zhong, W. Zhu, A. Lin and M. S. El-Shall, Synergetic catalysis of palladium nanoparticles encaged within amine-functionalized UiO-66 in the hydrodeoxygenation of vanillin in water, *Green Chem.*, 2016, **18**, 2900–2908.

52 M. Manafi Moghadam, A. Ramazani, A. Morsali and S. Rezayati, Functionalization of Magnetic UiO-66-NH_2 with Schiff Base Copper(II) Complex for the One-Pot Synthesis of Pyran-Annulated Heterocyclic Scaffolds, *Inorg. Chem.*, 2025, **64**, 8016–8030.

53 S. Safaei, S. Tangestaninejad, M. Moghadam, M. Bahadori, I. Mohammadpoor-Baltork, A. Omidvar and M. Mirzaeian, Straightforward linker functionalization in UiO-66-NH_2 via Schiff-base condensation with metal acetylacetonate complex: a post-modification approach toward heterogeneous catalytic epoxidation, *J. Ind. Eng. Chem.*, 2025, DOI: **10.1016/j.jiec.2025.06.053**.

54 F. Kiani, D. Elhamifar and S. Kargar, Magnetic resorcinol-formaldehyde supported isatin-Schiff-base/Fe as a green and reusable catalyst for the synthesis of pyrano[2,3-d] pyrimidines, *Nanoscale Adv.*, 2025, **7**, 1552–1560.

55 F. Dadvar and D. Elhamifar, A Pd-containing ionic liquid modified magnetic graphene oxide nanocomposite (Fe_3O_4/GO–IL–Pd) as a powerful catalyst for the reduction of nitrobenzenes, *Nanoscale Adv.*, 2024, **6**, 5398–5408.

56 G. Antarnusa, P. D. Jayanti, Y. R. Denny and A. Suherman, Utilization of co-precipitation method on synthesis of Fe_3O_4/PEG with different concentrations of PEG for biosensor applications, *Materialia*, 2022, **25**, 101525.

57 S. Kargar and D. Elhamifar, UiO-66-NH_2 metal–organic framework supported palladium/Schiff-base complex as a highly efficient and robust catalyst for the Suzuki reaction, *Nanoscale Adv.*, 2025, **7**, 4194–4204.

58 J. Zhang, Y. Hu, J. Qin, Z. Yang and M. Fu, TiO_2-UiO-66-NH_2 nanocomposites as efficient photocatalysts for the oxidation of VOCs, *Chem. Eng. J.*, 2020, **385**, 123814.

59 M.-A. Rezaie, A. Khojastehnezhad and A. Shiri, Post-synthetic modification of Zr-based metal organic framework by Schiff base zinc complex for catalytic applications in a click reaction, *Sci. Rep.*, 2024, **14**, 24644.

60 D. C. Gowda and B. Mahesh, Catalytic transfer hydrogenation of aromatic nitro compounds by employing ammonium formate and 5% platinum on carbon, *Synth. Commun.*, 2000, **30**, 3639–3644.

61 M. Dabiri, H. Fazli, N. Salarinejad and S. K. Movahed, Pd nanoparticles supported on cubic shaped ZIF-based materials and their catalytic activates in organic reactions, *Mater. Res. Bull.*, 2021, **133**, 111015.

62 X.-P. Feng, Y.-F. Guo, R. Qian, B. Deng, Z. Chen, B. Yang and R. Yang, Immobilized β-cyclodextrin and palladium-pyridylaldehyde complex on silica nanoparticles as a highly active catalyst for Suzuki, reduction of nitroarenes and oxidative amination of aldehydes reactions in water, *Mater. Today Commun.*, 2021, **26**, 101909.

63 M. Gholinejad, F. Zareh and C. Nájera, Nitro group reduction and Suzuki reaction catalysed by palladium supported on magnetic nanoparticles modified with carbon quantum dots generated from glycerol and urea, *Appl. Organomet. Chem.*, 2018, **32**, e3984.

64 Y. Xu, W. Shan, X. Liang, X. Gao, W. Li, H. Li and X. Qiu, Cobalt Nanoparticles Encapsulated in Nitrogen-Doped Carbon Shells: Efficient and Stable Catalyst for Nitrobenzene Reduction, *Ind. Eng. Chem. Res.*, 2020, **59**, 4367–4376.

65 J. Rahimi, R. Taheri-Ledari, M. Niksefat and A. Maleki, Enhanced reduction of nitrobenzene derivatives: effective strategy executed by Fe_3O_4/PVA-10%Ag as a versatile hybrid nanocatalyst, *Catal. Commun.*, 2020, **134**, 105850.

66 S. Sobhani, F. O. Chahkamali and J. M. Sansano, A new bifunctional heterogeneous nanocatalyst for one-pot reduction-Schiff base condensation and reduction–carbonylation of nitroarenes, *RSC Adv.*, 2019, **9**, 1362–1372.